Structural and Multidisciplinary Optimization (2025) 68:254
https://doi.org/10.1007/s00158-025-04201-w

RESEARCH PAPER

Optimization of non-closed multi-cell hexagonal columns generated through topology optimization for enhanced crashworthiness under multiple load angles

VanThanh Dang[1] · Michal Rogala[2] · Ameen Topa[3] · PhucThien Nguyen[4] · TrongNhan Tran[5]

Received: 18 February 2025 / Revised: 12 September 2025 / Accepted: 9 November 2025

Abstract
While traditional or bio-inspired multi-cell structures are widely utilized for crashworthiness applications, this study explores the performance of novel non-closed multi-cell hexagonal columns (NMHCs) with section geometries developed through topology and multi-objective optimizations. Experimental tests, serving as a foundation for validating numerical simulations, were conducted to analyze the behavior of NMHCs under varying loading angles (0°, 10°, and 20°). Four specific configurations (II-NMHC1.4–90-20, II-NMHC1.8–90-20, III-NMHC1-90–20, and III-NMHC1.4–90-20) demonstrated progressive deformation under a 20° oblique impact, with thicker walls preferred for II-NMHC and thinner walls for III-NMHC to achieve optimal performance. Notably, SEA for these four columns decreased by an average of 29% under oblique impact, whereas other configurations experienced a 61.5% reduction compared to axial loading. Cell number, load angle, and section geometry significantly influenced peak load and specific energy absorption, while wall thickness and diameter primarily affected peak load. Optimization results further highlighted optimal performance at a 10° loading angle across all configurations. The III-NMHC outperformed its peers with identical features, achieving the smallest peak load and highest energy absorption.

Keywords Crashworthiness and Topology optimization · Non · Closed multi · Cell thin · Walled tube · Energy absorption · Axial and oblique impact

1 Introduction

The surge in road traffic accidents, primarily driven by the proliferation of private vehicles, has necessitated enhanced safety measures. Consequently, energy absorption devices and warning systems are being integrated to improve passive safety and mitigate fatalities and severe injuries in automobile accidents.

Crash boxes, particularly those utilizing tubular metals based on thin-walled tubes, have emerged as promising lightweight structures for impact energy absorption. These designs boast an exceptional energy absorption-to-mass ratio (Olabi et al. 2007), making them ideal for automotive applications. However, ongoing technological advancements underscore the need for further enhancements to their energy absorption efficiency (Lam et al. 2023).

Studies reveal that thin-walled columns exhibit progressive deformation under axial impact (Xu et al. 2018) and oblique impact with minimal load angles (Qi et al. 2012), whereas large load angles induce global bending (Tarlochan et al. 2013). Notably, their primary energy-absorbing mechanism involves irreversible plastic deformation and/or tearing (Reid 1993), emphasizing the importance of optimized design.

Extensive research has been conducted on the crashworthiness of thin-walled structures, employing diverse methods such as theoretical modeling, numerical simulation, and

Responsible Editor: Axel Schumacher.

✉ TrongNhan Tran
trantrongnhan@iuh.edu.vn

[1] Ca Mau Department of Construction, Ca Mau, Vietnam

[2] Faculty of Mechanical Engineering, Lublin University of Technology, Lublin, Poland

[3] Department of Maritime Technology, Faculty of Ocean Engineering Technology, Universiti Malaysia Terengganu, Kuala Terengganu, Malaysia

[4] Van Hien University, 665-667-669 Dien Bien Phu St, Ban Co Wd, Ho Chi Minh City, Vietnam

[5] Faculty of Mechanical Engineering, Industrial University of Ho Chi Minh City, Ho Chi Minh City, Vietnam

Published online: 20 November 2025

experimentation. Notably, Chen and Wierzbiecki (Chen and Wierzbicki 2001) adapted the super folding element theory to predict the mean collapsing force of axially impacted thin-walled square tubes, while Tran et al. (Tran et al. 2014) expanded this theory to encompass oblique impacts.

Complementary experimental studies have provided valuable insights. For instance, Alavi Nia and Parsapour (Alavi Nia and Parsapour 2014) investigated the energy absorption responses of thin-walled tubes with varying cross-sectional configurations under quasi-static loading, revealing that multi-cell tubes require greater energy to fold due to additional blades. Additionally, Tran et al. (Tran et al. 2020) examined the crashworthiness characteristics of tube-nested structures subjected to lateral compression, highlighting the critical role of inner tubes in resisting compression.

Numerical simulation methods dominate the literature, offering detailed analyses. Yang et al. (Yang et al. 2019) utilized numerical simulations to investigate the failure and crashworthiness performance of frustum sandwich structures, elucidating the impact of structural parameters on crashworthiness indexes. Isaac and Oluwole (Isaac and Oluwole 2018) employed finite element simulations to explore the behavior and energy absorption characteristics of singular tubes under axial and oblique impacts, demonstrating the superior crashworthiness of hexagonal tubes with vertical grooves. Furthermore, Nikkhah et al. (Nikkhah et al. 2017) leveraged finite element modeling to investigate the influence of hole shape on tube crashworthiness, concluding that square and rectangular holes substantially impair tube integrity.

Numerous studies focus on optimizing thin-walled tubes, paralleling simulation research. Pirmohammad and Esmaeili-Marzdashti (Pirmohammad and Esmaeili-Marzdashti 2019) conducted multi-objective optimization of multi-cell tubes with varying hole configurations, demonstrating enhanced crashworthiness indexes. Huang and Xu (Huang and Xu 2019) optimized multi-cell tubes under combined axial and oblique loading, utilizing weighting factors to determine optimal solutions. Further advancing this field, Booth et al. (Booth et al. 2021) employed an adaptive surrogate-assisted response surface method in their optimization of multi-cell rails under diverse loading conditions, demonstrating the method's effectiveness in accurately characterizing the Pareto set. Beyond multi-objective optimization, topology optimization serves as a pivotal initial design step toward achieving optimal solutions (Aulig et al. 2018). Typically, topology optimization addresses canonical problems, such as cantilever design (Liu et al. 2017) and Messerschmitt-Bölkow-Blohm beam optimization (Latifi Rostami and Ghoddosian 2019), illustrating its versatility.

Recent studies have demonstrated the significant potential of section configurations in enhancing thin-walled column crashworthiness, with cross-sectional design being fundamentally driven by structural constraints and functional requirements. The selection of cross-sectional geometries predominantly follows two distinct approaches: conventional geometric configurations, encompassing triangular (Tran and Baroutaji 2018), square (Arnold and Altenhof 2004), pentagonal (Ali et al. 2015), hexagonal (Deng et al. 2024), octagonal (Zhang et al. 2018), polygon (Jiang et al. 2024), and circle (Peng et al. 2024) shapes; and bio-inspired structures that emulate natural formations, such as bionic honeycomb columns (Xiang and Du 2017), lotus root-filled configurations (Li et al. 2018), multi-cell columns inspired by beetle elytron microstructure (Yu et al. 2019), cactus-inspired multi-cell tube (Chen et al. 2024a), and design based on Morpho butterfly wing architecture (Nikkhah et al. 2020). While existing literature extensively explores these traditional and bio-inspired sections, the critical requirement for energy absorbers to maintain sufficient rigidity for progressive deformation while resisting bending under oblique impact necessitates further investigation.

To address these challenges, this study advances the field through comprehensive examination of non-closed structures under multi-load angle conditions, employing an innovative dual-optimization approach that integrates topology optimization for section geometry development with multi-objective optimization techniques. This systematic methodology facilitates the design of optimized crashworthy structures, with performance evaluation encompassing behavioral characteristics, load response patterns, and energy absorption capabilities. Furthermore, the investigation explores the interrelationship between loading conditions, column parameters, and crashworthiness performance, with particular emphasis on determining effective load angles for optimal structural response.

2 Methodology

The design optimization of collision-subjected structures demands a delicate balance between achieving stable, progressive, and controlled deformation patterns while maximizing the critical energy absorption-to-mass ratio. Building upon McGregor et al's (McGregor et al. 1993) demonstration that cross-sectional geometry fundamentally governs crashworthiness performance, this methodology integrates both topology optimization and multi-objective size optimization as essential components of the design process. Through sophisticated topology optimization techniques, design concepts are systematically generated to satisfy predetermined constraints and requirements, thereby facilitating optimal energy absorption characteristics and deformation behavior. As depicted in Fig. 1, this comprehensive design framework progresses through several interconnected phases: topology optimization

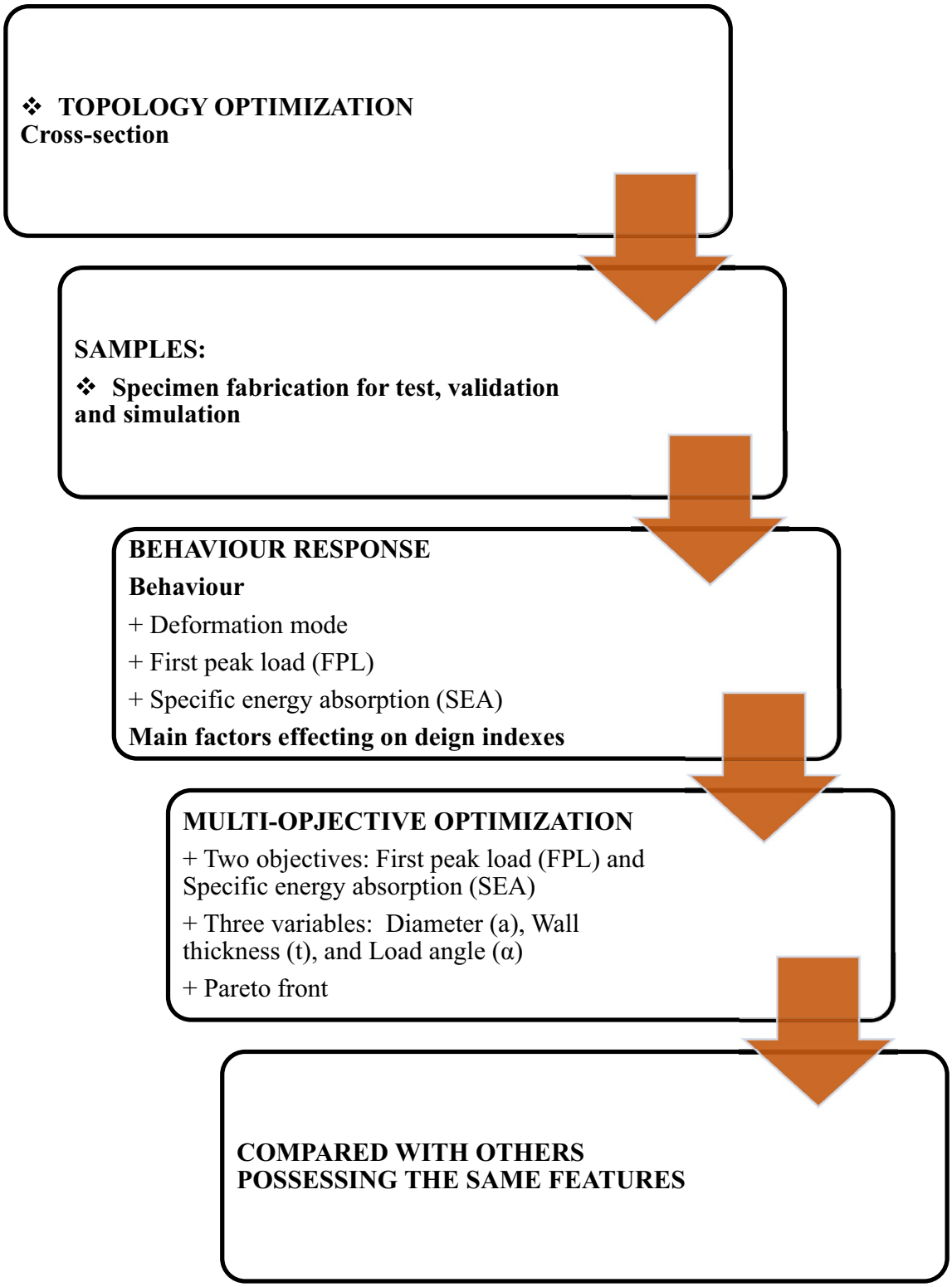

Fig. 1 Design process

defines the structure's cross-sectional configuration, followed by specimen fabrication for test, validation and simulation, and subsequent assessment of key performance metrics—including deformation mode, first peak load (FPL), and specific energy absorption (SEA). The process culminates in a Pareto set through multi-objective

optimization, identifying optimal design solutions. Finally, the optimized design is compared with other structures having similar features to assess its performance.

2.1 Structure geometry

The fundamental topology optimization problem (Aulig et al. 2018), as depicted in Fig. 1, can be mathematically expressed through the following relationship:

$$\begin{aligned} &\min_{\rho} F = F(u,\rho) \\ &s.t. \quad : G(\rho) = \int_{\Omega} g(x,\rho)dV - V_0 \le 0 \\ &\qquad : K(\rho)u = f \\ &\qquad : 0 \le \rho(x) \le 1 \end{aligned}, \tag{1}$$

wherein u represents the state field satisfying the equilibrium equations, $K(\rho)$ is the stiffness matrix dependent on the density distribution $\rho(x)$, f is the load vector, and V_0 denotes the maximum allowable material volume. The design variable $\rho(x)$ is the material density field, where $\rho = 0$ corresponds to void and $\rho = 1$ to solid material.

Topology optimization aims to determine the optimal material distribution within a prescribed design domain Ω that minimizes the objective function (e.g., compliance, strain energy, or crashworthiness-related indices) while satisfying equilibrium and volume constraints. A widely used interpolation approach for relating material properties to density is the Solid Isotropic Material with Penalization (SIMP) method (Bendsøe and Sigmund 2004):

$$E(\rho) = \rho^p E_0, \tag{2}$$

where $E(\rho)$ is the effective Young's modulus, E_0 is the modulus of the base material, and $p > 1$ is a penalization factor that suppresses intermediate densities, driving the solution toward a distinct solid–void configuration.

The NMHCs were developed through topology optimization applied to a circular design domain of diameter a, subject to a volume fraction constraint of 15–25%. The domain was loaded in traction with the bottom boundary fully constrained. After 100 iterations with a convergence tolerance of 0.01%, the optimal density distribution evolved into a hexagonal configuration with internal non-closed cells, as shown in Fig. 2a. These patterns formed the basis for three design variants, categorized as I-NMHC (four cells), II-NMHC (six cells), and III-NMHC (seven cells), as illustrated in Fig. 2b. To facilitate classification, a systematic nomenclature was adopted (e.g., II-NMHC1.4–80-10 denotes a subgroup II specimen with a 1.4 mm wall thickness, 80 mm diameter, and a 10° loading angle). The geometrical parameters of all variants are summarized in Table 1.

2.2 Finite element model (FEM)

Due to the complexity and high cost associated with specimen fabrication and experimentation, this study employs finite element analysis (FEA) to investigate the behavior of non-closed multi-cell hexagonal columns (NMHCs) under multi-angle impact loading. Previous research indicates that under axial loading (0°), tubes exhibit the canonical progressive folding deformation mode (Cai and Deng xxxx), under small oblique loading (10°), progressive folding remains dominant (Li et al. 2019), and under large oblique loading (20°), global bending and buckling tendencies begin to emerge (Qin et al. 2024). Additionally, tubes subjected to loading conditions of 30° or greater often experience global bending and a significant loss of load-bearing capacity (Xiong et al. 2022). Accordingly, three representative loading angles—0°, 10°, and 20°—were selected as anchor points to capture distinct deformation regimes, from axial folding through transitional folding to the onset of global buckling. These angles are therefore sufficient to characterize the key crashworthiness responses of NMHCs within the range of interest.

The test set-up, illustrated in Fig. 3a, involves fixing the bottom end of each NMHC specimen to a rigid wall with all degrees of freedom constrained. A 600 kg moving wall (Chen et al. 2024b) applies an axial load to the free end at angles of $\alpha = 0°$ (0 rad), 10° (0.1745 rad), and 20° (0.349 rad). Both the moving and fixed walls are modeled using rigid material type 20 in the LS-Dyna solver. The NMHC specimens are discretized using four-node Belytschko-Tsay shell elements, with an elastic–plastic material model (MAT24) and a friction coefficient of 0.2 applied at contact interfaces (Cai and Deng xxxx).

The test specimens were fabricated from AA6061-O alloy, with identical manufacturing and heat treatment processes applied to both tensile samples and crash tubes to ensure consistency. Mechanical properties were determined as the average of three tensile tests, with the corresponding specimens and stress–strain curve shown in Fig. 3b. The alloy exhibited an elastic modulus of 68.5 GPa, a density of 2700 kg/m^3, a Poisson's ratio of 0.3, and a yield stress of 39.27 MPa. As AA6061-O demonstrates rate-independent behavior within the strain-rate range of 10^{-3} to 10^3 s^{-1} (Qin et al. 2024), strain-rate effects were considered negligible and omitted from the simulations.

To evaluate the crashworthiness of thin-walled tubes under dynamic loading, previous studies commonly employed an impact velocity of 15.6 m/s. For instance, Tarlochan et al. (Tarlochan et al. 2013) examined various thin-walled tubes at this impact speed. Accordingly, an impact velocity of 15.6 m/s is adopted for this investigation. Automatic single-surface and automatic surface-to-surface contact algorithms are employed to simulate self-contact

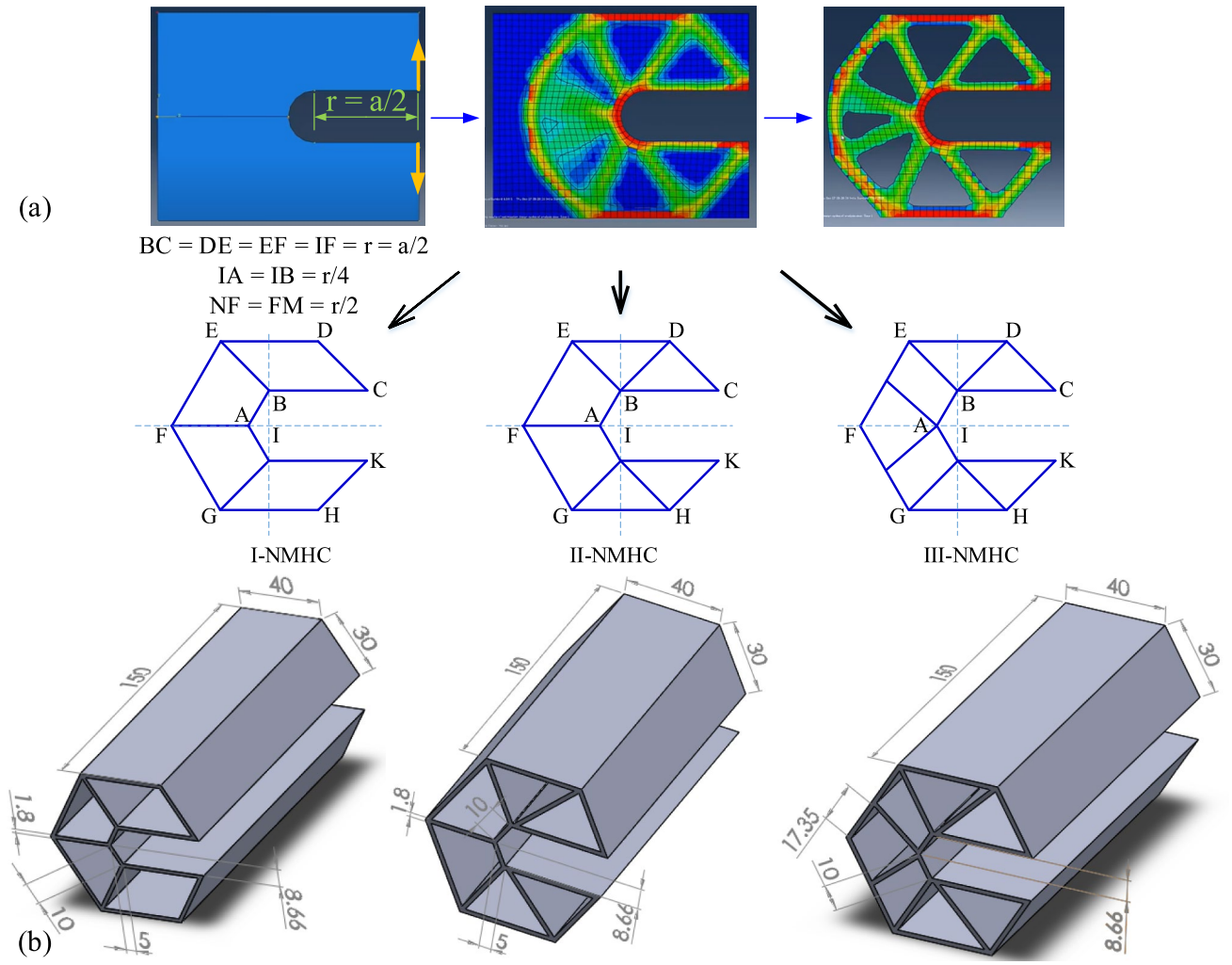

Fig. 2 **a** Optimal cross-sectional geometry and **b** non-closed multi-cell hexagonal columns (NMHCs)

within NMHCs and contact between NMHCs and the wall, respectively.

The computational investigation of the NMHC model necessitated a comprehensive mesh size sensitivity analysis, wherein five distinct element sizes were systematically evaluated to ascertain their intricate influence on peak load and energy absorption. As illustrated in Fig. 4, the element sizes demonstrate a markedly impact on energy absorption, with more pronounced variations compared to peak load. Comparative analyses revealed variations in energy absorption across different element sizes. Specifically, when juxtaposing an element size of 1.4 mm against other sizes, the energy absorption differentials were quantified: relative to the baseline, the 2 mm and 1.8 mm sizes exhibited marginal deviations of 2.72% and 1.42%, respectively. Conversely, the 2.8 mm element size demonstrated a more substantial divergence, registering a 5.57% deviation from the reference configuration. Complementing the energy absorption analysis, computational efficiency metrics were concurrently examined. The temporal computational requirements for the 1.4 mm element size were observed to be significantly more demanding, ranging from 1.54 to 5.51 times the computational resources necessitated by other element sizes. Following comparative evaluation, the 2 mm element size was ultimately selected as the optimal configuration for subsequent simulations, balancing computational efficiency with precision of outcomes.

2.3 Verification of FEM

Prior to conducting the analysis, the establishment of an appropriate finite element method (FEM) construction for simulation necessitates two fundamental steps: mesh generation and FEM validation, both of which are crucial for ensuring computational accuracy. In the development of the I-NMHC model, five distinct element sizes—1.5, 2.0, 2.5,

Table 1 Data of three subgroups under impact

Subgroup				I-NMHC				II-NMHC				III-NMHC			
n	t (mm)	a (mm)	Alpha (°)	m (kg)	EA (kJ)	FPL (kN)	SEA (kJ/kg)	m (kg)	EA (kJ)	FPL (kN)	SEA (kJ/kg)	m (kg)	EA (kJ)	FPL (kN)	SEA (kJ/kg)
1	1.0	70	0	0.1910	4.062	17.481	21.269	0.2245	4.996	20.542	22.253	0.2352	5.522	21.722	23.476
2			10		3.845	4.187	20.129		4.427	4.981	19.720		5.006	4.539	21.282
3			20		1.396	2.098	7.309		1.540	2.101	6.861		1.655	2.346	7.035
4	1.0	80	0	0.2186	4.213	20.165	19.273	0.2571	5.229	23.753	20.337	0.2693	5.810	24.977	21.575
5			10		3.730	4.186	17.064		4.565	4.864	17.757		5.240	4.521	19.457
6			20		1.769	2.112	8.094		1.926	2.118	7.490		2.419	2.226	8.984
7	1.0	90	0	0.2463	4.365	22.869	17.723	0.2896	5.317	26.893	18.359	0.3034	6.190	28.324	20.403
8			10		3.814	4.281	15.487		4.664	4.873	16.105		4.664	4.873	15.372
9			20		2.139	2.128	8.686		2.884	2.112	9.959		4.421	2.122	14.570
10	1.4	70	0	0.2658	7.080	23.928	26.635	0.3125	8.376	28.459	26.803	0.3274	9.305	29.534	28.420
11			10		6.456	7.264	24.289		7.559	7.997	24.188		8.368	7.085	25.558
12			20		2.357	2.174	8.866		2.670	3.117	8.543		2.988	4.162	9.128
13	1.4	80	0	0.3045	7.386	27.545	24.258	0.3581	8.701	32.479	24.296	0.3751	9.935	34.043	26.485
14			10		6.713	7.577	22.046		7.756	8.143	21.659		8.691	8.723	23.169
15			20		2.831	3.625	9.297		3.121	4.115	8.715		3.689	4.101	9.836
16	1.4	90	0	0.3433	7.571	31.543	22.055	0.4037	8.998	36.769	22.288	0.4228	10.205	38.835	24.136
17			10		6.678	7.906	19.453		8.194	8.684	20.298		8.902	8.856	21.054
18			20		3.567	3.374	10.390		6.376	4.422	15.794		7.230	4.334	17.100
19	1.8	70	0	0.3397	10.404	29.785	30.627	0.3995	11.828	35.159	29.606	0.4185	13.177	37.080	31.487
20			10		9.445	10.952	27.804		10.792	12.219	27.014		12.175	10.568	29.093
21			20		3.438	5.808	10.121		3.700	7.143	9.260		4.160	7.102	9.941
22	1.8	80	0	0.3896	10.522	34.421	27.007	0.4581	13.252	40.568	28.928	0.4798	13.617	43.327	28.381
23			10		10.147	11.843	26.045		11.427	12.228	24.944		11.427	11.242	23.816
24			20		4.532	6.219	11.633		4.565	6.127	9.966		5.249	6.103	10.939
25	1.8	90	0	0.4394	10.905	39.116	24.818	0.5166	13.336	46.068	25.815	0.5412	14.418	48.399	26.641
26			10		10.083	12.302	22.948		11.721	12.308	22.689		12.807	11.289	23.664
27			20		5.168	6.693	11.762		9.504	7.134	18.397		8.011	7.086	14.803

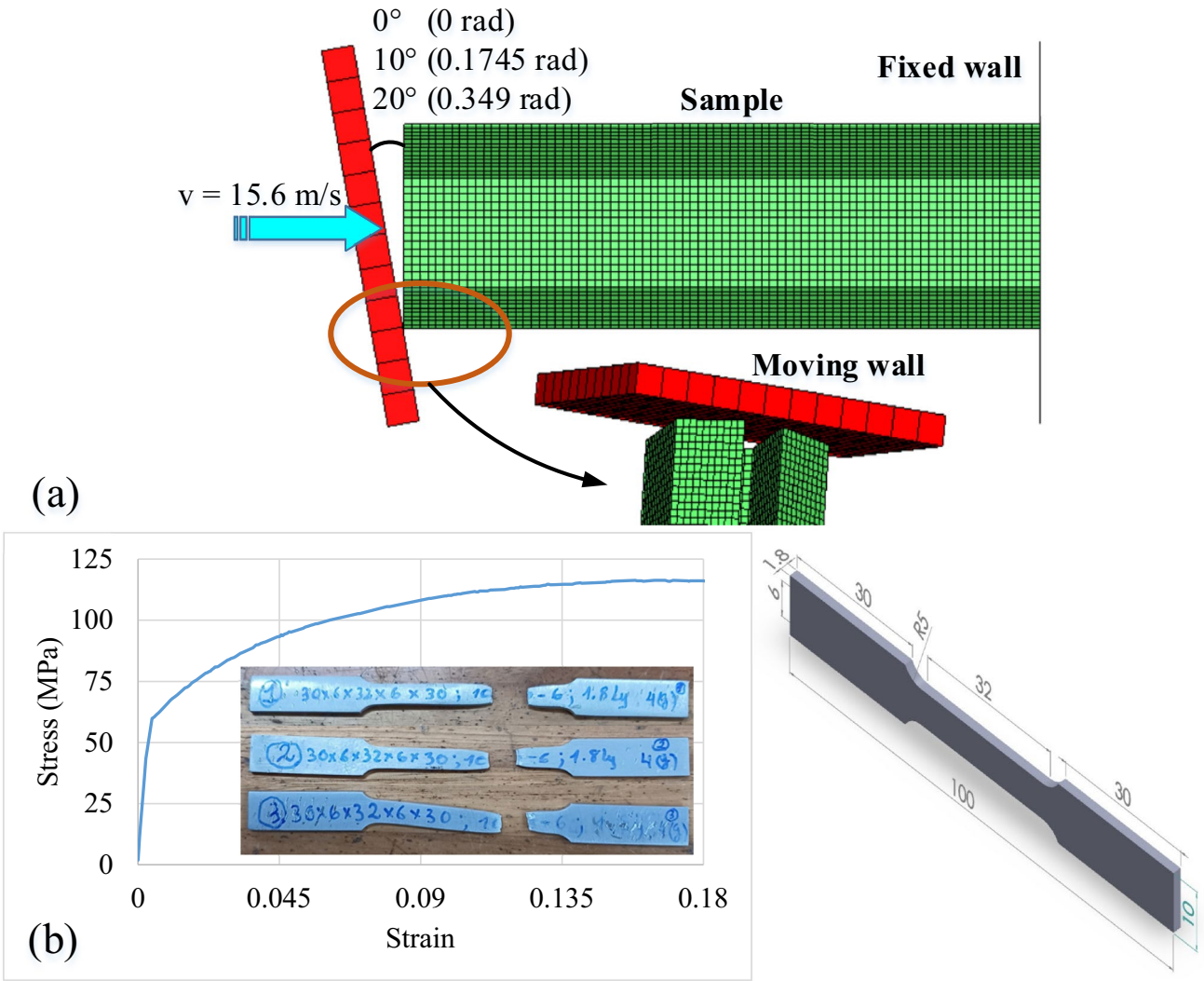

Fig. 3 **a** Test set-up and detail loading cases and **b** Stress–strain curve

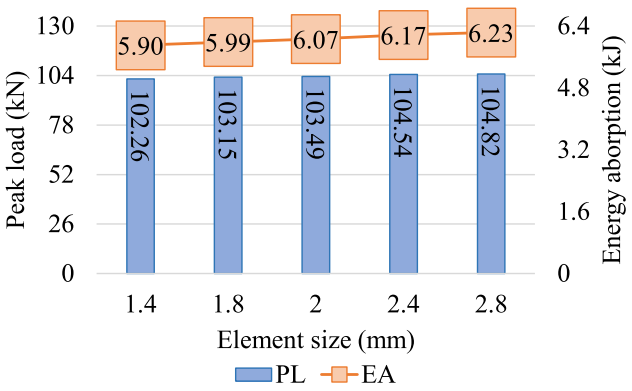

Fig. 4 Mesh convergence analysis

3.0, and 3.5 mm—were systematically evaluated, with the resultant peak loads illustrated in Fig. 4, wherein the element sizes of 1.5 and 2.0 mm demonstrated minimal variations of 2.76 and 1.17%, respectively, when compared to the 2.5 mm baseline. The convergence analysis revealed that as the element size decreased, the peak load exhibited increasing stability and consistency, which, coupled with Waleed et al. 's (Waleed et al. 2023) findings regarding the optimal 2.0 mm element size for crushing analysis, led to the adoption of this element size for simulating the novel non-closed multi-cell hexagonal columns' crushing behavior.

The experimental specimens were fabricated using wire-cut electrical discharge machining (WEDM), as illustrated in Fig. 5a. This technique was selected for its ability to produce precise and complex internal geometries with minimal material distortion. In WEDM, a continuously moving fine metal wire serves as the electrode, eroding material

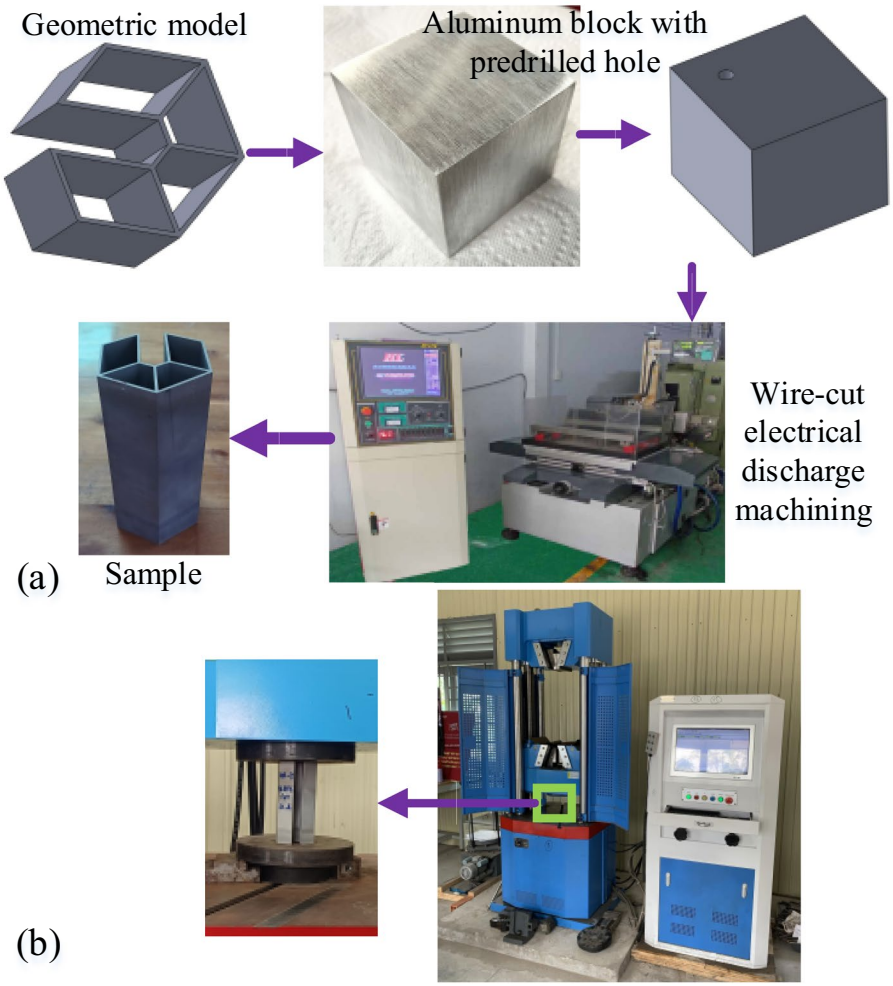

Fig. 5 **a** Fabrication process and **b** Experimental test

from a conductive workpiece through controlled electrical discharges.

The accuracy of the finite element model (FEM) was validated against experimental results obtained from two specimens, I-NMHC and II-NMHC. Compression tests were conducted on a hydraulic universal testing machine (WEW-1000B, Wuxi New Luda Instrument Co., Ltd., China), equipped with a 1000 kN load cell with ± 1% full-scale accuracy, as shown in Fig. 5b. A constant loading rate of 3 mm/min was applied. Corresponding FEM simulations were performed at a compressive velocity of 1 m/s (Gong et al. 2023) to optimize computational efficiency while maintaining accuracy. These simulations were considered quasi-static, as the internal-to-kinetic energy ratio remained below 5%.

The comparative analysis between experimental and numerical results, shown in Fig. 6, demonstrates strong agreement for both I-NMHC and II-NMHC configurations. Both exhibit the characteristic threefold in-extensional deformation mode, with only minor differences in the final folded shapes. These discrepancies are attributable to physical testing factors, such as slight manufacturing imperfections and load eccentricities, which are absent in the idealized numerical model.

In crashworthiness terms, deformation is governed by the formation of plastic hinges and progressive folding. Under axial loading, outward bulges develop at the junctions of non-closed cells, where stress concentrations trigger localized buckling. These bulges propagate symmetrically along the tube length, producing a stable three-lobe folding mode that ensures uniform energy dissipation. Under oblique loading, however, the deformation becomes increasingly asymmetric: bulges shift toward the loaded side, inclined plastic hinges form, and tilted folding bands promote localized collapse. As the loading angle increases, the instability intensifies, leading to premature buckling and reduced peak load and specific energy absorption. This behavior highlights the sensitivity of NMHC crashworthiness to loading orientation, with thicker-walled or higher-cell variants exhibiting greater resistance to asymmetric folding.

Despite minor geometric variations, both experimental and numerical results capture the same progressive folding

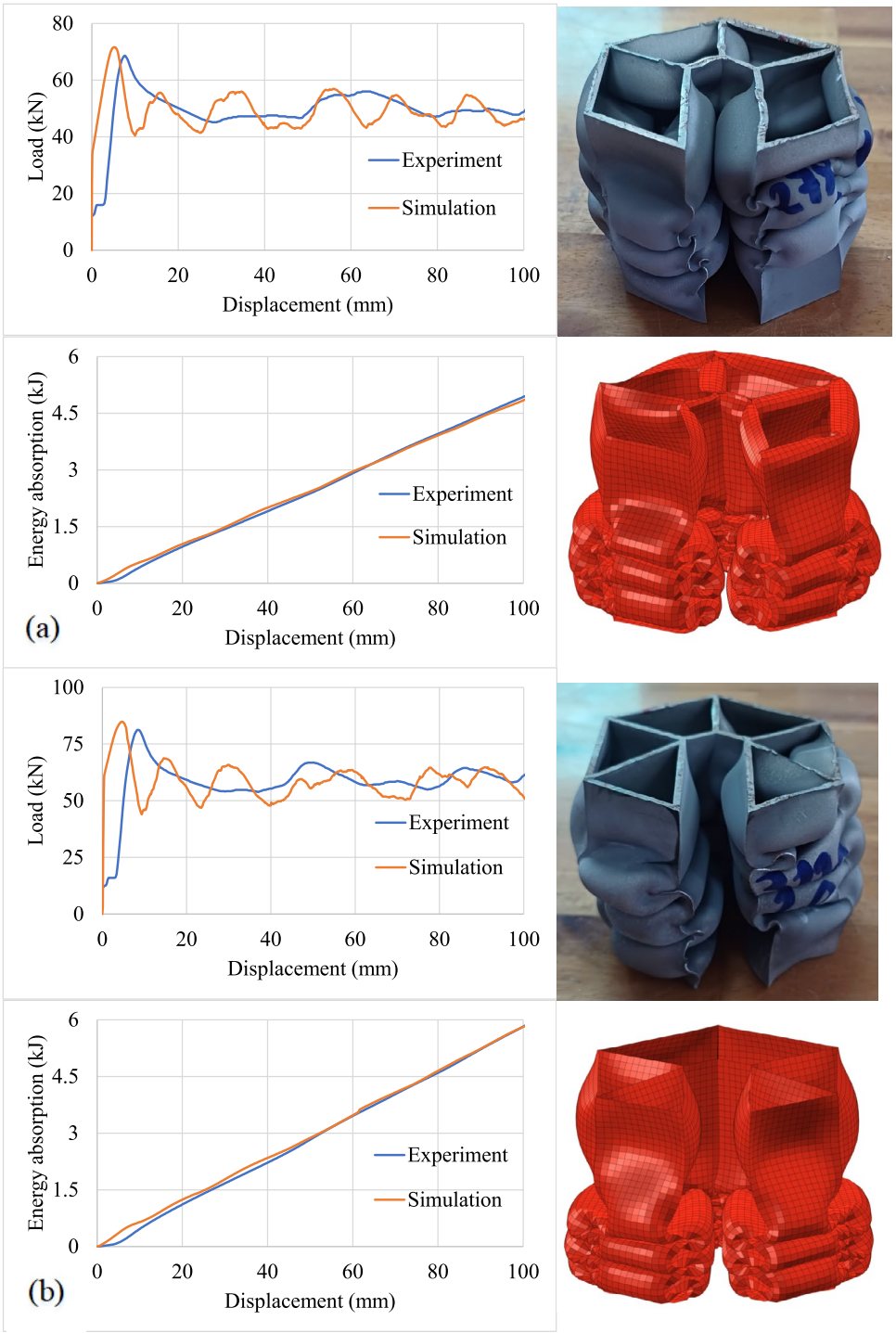

Fig. 6 Verification of FEM: **a** I-NMHC and **b** II-NMHC

sequence and energy absorption characteristics throughout the crushing process. The high correlation between load–displacement and energy absorption curves, with absolute errors in peak load and absorbed energy below 4.5%, confirms the reliability of the FEM under axial loading. This successful validation provides a solid foundation for applying the model to oblique impact scenarios, thereby establishing its robustness for subsequent analyses.

2.4 Design indexes

The comparative analysis of crash force diagrams serves as a definitive method for evaluating the efficacy of energy-absorbing devices, wherein critical parameters—including First Peak Load (FPL), Specific Energy Absorption (SEA), and Energy Absorption (EA)—are systematically extracted and analyzed (Hou et al. 2008). Within the force diagram,

FPL, which correlates directly with material elasticity, serves as a crucial indicator of the onset of plastic deformation; however, elevated FPL values can precipitate severe deceleration during impact events, potentially resulting in catastrophic consequences for vehicle occupants (Hou et al. 2011). Consequently, the optimization of crash energy-absorbing devices necessitates a delicate balance between minimizing peak load while maximizing energy absorption capacity.

The total internal energy absorbed throughout the crash event, denoted as EA (Chen et al. 2022), can be mathematically expressed through the integral relationship:

$$EA = \int F_{in} d\delta_{cd}, \tag{3}$$

where F_{in} represents the crash force and δ_{cd} denotes the corresponding displacement. In evaluating structural efficiency, SEA (Chen et al. 2023) emerges as a fundamental parameter, calculated as the ratio between energy absorption and structural mass (m):

$$SEA = \frac{\int F_{in} d\delta_{cd}}{m} \tag{4}$$

The comprehensive assessment of structural crashworthiness incorporates two additional parameters that are intrinsically linked to crash load characteristics and energy absorption capacity: First Peak Load Efficiency (FPLE) and Specific Energy Absorption Efficiency (SEAE). These parameters are quantified through the following mathematical expressions:

$$FPLE = 100\% \frac{FPL_{\alpha_i} - FPL_{\alpha_0}}{FPL_{\alpha_0}} \tag{5}$$

$$SEAE = 100\% \frac{SEA_{\alpha_i} - SEA_{\alpha_0}}{SEA_{\alpha_0}}, \tag{6}$$

where FPL_{α_0} and SEA_{α_0} represent the First Peak Load and Specific Energy Absorption, respectively, at a load angle of 0°, while FPL_{α_i} and SEA_{α_i} correspond to their respective values at load angles of either 10° or 20°.

3 Optimization

In the context of crash absorption systems, the fundamental design challenge lies in the inherent contradiction between two critical factors: the structure must maximize impact energy absorption while simultaneously minimizing peak load. This intrinsic trade-off necessitates careful consideration in the design process, as optimal crash box performance is characterized by the concurrent achievement of minimal peak load and maximal specific energy absorption (Hou et al. 2014). To address this complex optimization challenge, Multi-objective Optimization Design (MOOD) methodology is employed to generate a Pareto set of optimal solutions, from which specific configurations can be selected based on particular application requirements.

Analysis of the structural response, as illustrated in Fig. 6, reveals a significant observation: the maximum peak load manifests exclusively during axial impact scenarios, while being notably absent under oblique impact conditions. Consequently, FPL emerges as a critical objective function within the optimization problem. Following established design principles, the optimization problem is formulated with dual objectives: maximizing SEA while simultaneously minimizing or constraining FPL within predetermined parameters. The mathematical formulation of this optimization problem can be expressed as:

$$\begin{cases} \min : FPL = f_1(t, a, \alpha) \\ \max : SEA = f_2(t, a, \alpha) \\ s.t : \begin{cases} 1 \le t \le 1.8(mm) \\ 70 \le a \le 90(mm) \\ 0 \le \alpha \le 0.349(rad) \end{cases} \end{cases} \tag{7}$$

In this formulation $f_1(t, a, \alpha)$ and $f_2(t, a, \alpha)$ represent the objective functions for FPL and SEA, respectively, with respect to three key parameters: wall thickness (t), base circle diameter (a), and load angle (α). The general solution for these objective functions takes the form:

$$f(t, d, \alpha) = \sum_{i=0, j=0, k=0} \beta_{ijk} t^i d^j \alpha^k, \tag{7}$$

where $i, j,$ and$k$ denote the respective exponents of the variables in the polynomial expression.

4 Result and discussion

4.1 Structure behavior

When a structure is subjected to an impact load, it can experience two main types of deformation: progressive folding or global buckling mode. However, Albak Eİ (Albak 2021) has shown that under axial impact and oblique impact with a small load angle, the progressive folding mode is dominant over the global buckling one. This difference in deformation mode has a significant impact on the crushing load and energy responses of the structure. Notably, the progressive folding mode has been shown to absorb much more energy

than the global buckling mode by increasing the energy absorption capacity in a reliable way (Liu et al. 2021).

Figures 7 and 8 present the typical responses of NMHCs studied under multiple loading angle cases. The crushing load and EA responses for these NMHCs under the same loading cases exhibit similar behaviors (Fig. 7). Specifically, the load and EA responses for structures with different section geometries are quite similar to each other in the same loading case. This indicates that the section geometry has a relatively small influence on the overall crushing load and EA responses of the structure. These findings are important for the design and development of NMHCs as they suggest that the geometry can be optimized without significantly affecting the overall performance of the structure in impact loading scenarios.

As Fig. 8 illustrates, in the case of axial impact, the load response initially reaches its first peak, then falls slightly before suddenly rising again to its maximum peak load. Subsequently, it drops back and is followed by some fluctuations due to the successive formation of folds. In other words, the impact load increases quickly to a certain value and later fluctuates with a steady trend. On the other hand, in the case of oblique impact with a small load angle of 10°, the load response is comparable to that of axial impact in the later stages of the impact process. However, there is a difference in the early stage of the collision process, where the moving wall does not hit the structure's entire cross-section but instead strikes only the side of the tube's cross-section at the initial time. Unlike the axial impact condition, the maximum peak load disappears, and the collapsing load tends to increase slowly in the case of oblique impact. This phenomenon is caused by the structure partially wrinkling, while it fully wrinkles in the case of axial impact. The disappearance of the maximum peak load in the case of oblique impact with a small load angle demonstrates the advantage of this loading condition, which reduces fatalities in an impact event.

Figure 8 depicts that the load response during oblique impact with a load angle of 20° differs substantially from that during axial impact or oblique impact with a load angle of 10° due to the dominant global buckling mode. Specifically, during oblique impact with a load angle of 20°, the crash load increases at a slower rate, and the displacement at which the crash load reaches its maximum value is larger than that during axial impact or oblique impact with a load angle of 10°. In other words, the load behavior exhibits an

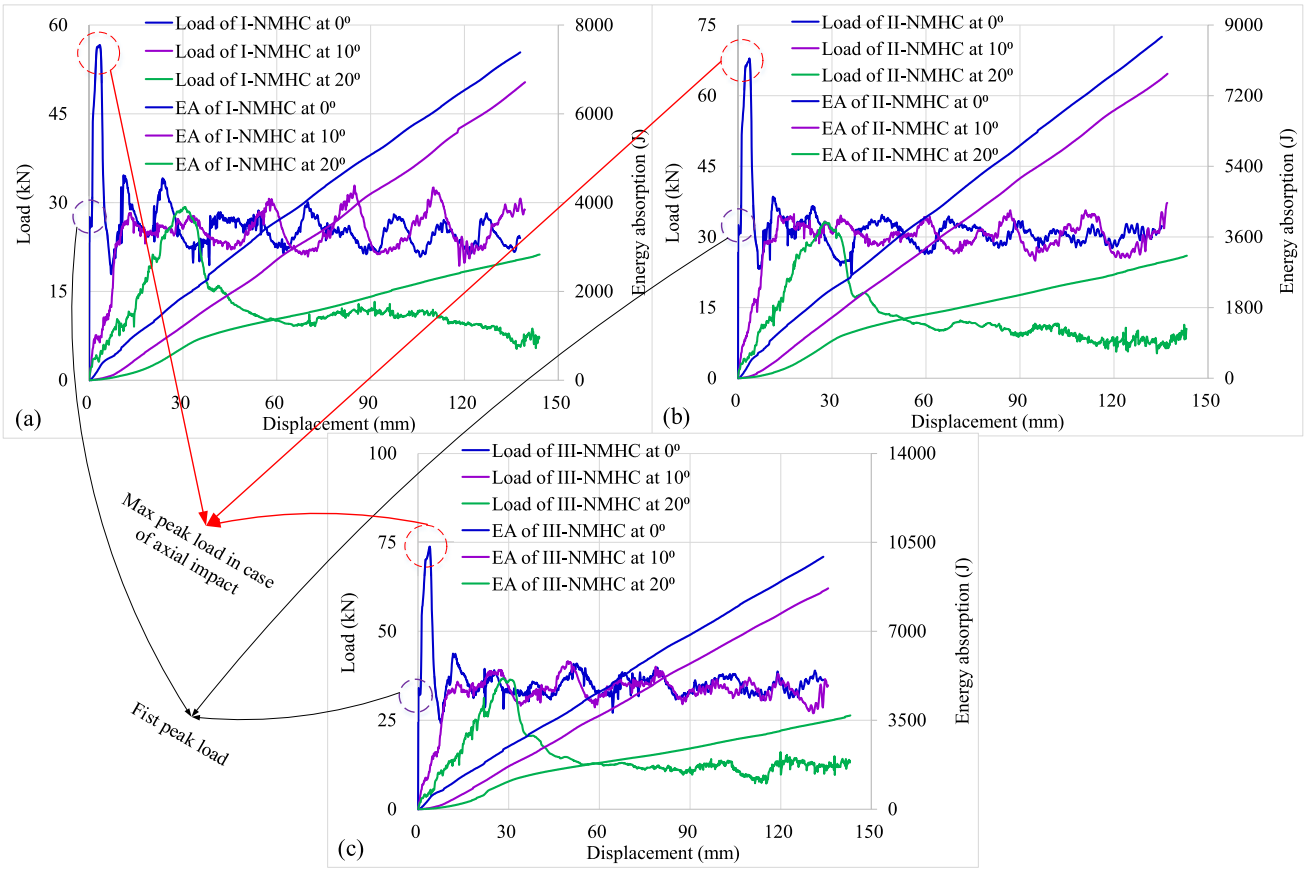

Fig. 7 Typical load and EA response at multi-loading angles of 0°, 10° and 20°: **a** I-NMHC, **b** II-NMHC, and **c** III-NMHC

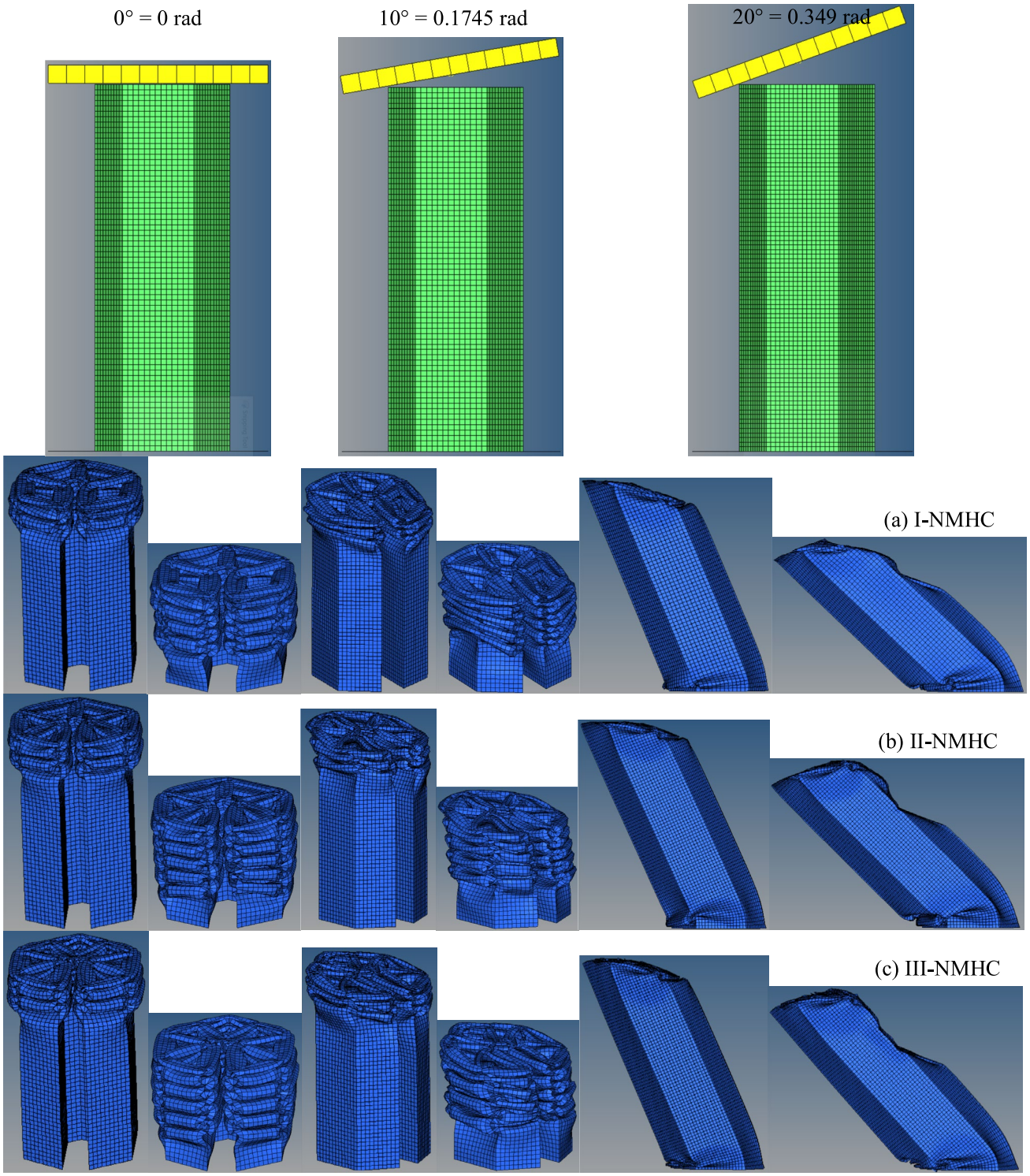

Fig. 8 Typical deformation response at multi-loading angles of 0°, 10° and 20°: **a** I-NMHC, **b** II-NMHC, and **c** III-NMHC

initial rise to the maximum value, followed by a gradual drop. This is because oblique impact with a larger load angle causes the deformation mode to shift from progressive folding to global buckling, which is recognized as an inefficient deformation type in terms of energy absorption (Huang and Xu 2019).

Furthermore, although the range of load fluctuation is around 10 kN, the load levels differ among the NMHC

groups. The group III-NMHC has the highest load level, while the group I-NMHC has the smallest load level, indicating that it takes more energy to crumble the structure as the number of cells increases. For NMHCs with the same section geometry, the load fluctuations during the later stages of the impact process during oblique impact with a large load angle of 20° are narrower than those during axial impact or oblique impact with a small load angle of 10°, which is attributed to the growing deformation of the structure wall under impact.

The energy absorption (EA) of the structure was observed to increase linearly with crash time. However, the loading condition significantly affects the EA capacity of the structure. As per the findings of Ref. (Isaac and Oluwole 2018), the EAs decrease in the following order: axial impact ($\alpha = 0°$), oblique impact with a small load angle ($\alpha = 10°$), and oblique impact with a large load angle ($\alpha = 20°$). Moreover, for NMHCs subjected to oblique impact with a large load angle of 20°, there is a sharp decrease in EA due to the structure undergoing global buckling deformation.

Figure 8 shows that all three NMHCs undergo the same crushing behavior despite variations in their section geometries when subjected to different loading conditions. Under oblique impact with a small load angle of 10°, all three columns can absorb collision energy through progressive wrinkling similar to that observed in axial impact. Deformation modes of all types of NMHCs under axial impact and oblique impact with a small load angle of 10° display progressive folding, where deformation occurs from the upper end to the lower end of the tube, resulting in stable deformation. However, under oblique impact with a large load angle of 20°, NMHCs undergo a global buckling mode with plastic hinge lines at both tube ends. These deformation mechanisms are directly related to the structure's energy absorption capacity, with progressive folding being the most desirable mode throughout the impact process. Furthermore, greater stability under impact is observed as the column's number of cells increase.

While most NMHCs under oblique impact with a large load angle of 20° experience global bending mode, there are certain structures in groups II-NMHC and III-NMHC, such as II-NMHC1.4–90-20, II-NMHC1.8–90-20, III-NMHC1-90–20, and III-NMHC1.4–90-20, that do not undergo bending deformation and possess similar behavior (as shown in Fig. 9). This phenomenon shows that structures belonging to group II-NMHC prefer a thicker wall thickness while those belonging to group III-NMHC prefer a thinner one. As observed in Figs. 7 and 9, the load and EA response of these NMHCs under oblique impact with a large load angle of 20° are quite similar to their responses in the case of oblique impact with a small load angle of 10°; however, the corresponding position where the crash load reaches its maximum value is further away from the case of load angle of 10°. Their collapse modes are the progressive folding one, which is recognized as the efficient deformation type from an energy absorption capacity point of view (Song et al. 2020). Therefore, these structures have sufficient rigidity to resist bending and express progressive deformation during oblique impact with a large load angle. If the structures are too rigid or too soft, they will bend when subjected to an oblique load with a large load angle.

4.2 Main factors effecting on deign indexes

As depicted in Figs. 7 and 8, the columns within these three subgroups exhibit the similar behaviors when subjected to the same collision conditions due to the similarity in profile and parameters of the columns. The variation of crashworthiness indexes for all subgroups is described in Fig. 10 and Table 2. It is observed that both FPL and SEA behave consistently for all impact cases, decreasing as the load angle increases. However, the downward trends of FPL and SEA differ in the ranges of 0° to 10° and 10° to 20°. Specifically, FPL tends to decrease sharply as the load angle increases from 0° to 10° and then decreases slightly when the load angle increases from 10° to 20℃. In contrast, SEA decreases slightly as the load angle increases from 0° to 10° and then decreases sharply as the load angle increases from 10° to 20°. For instance, when the load angle increases from 0° to 10° and 20°, FPL of III-NMHC1.8–80 decreases by 74.053 and 85.913%, respectively, while its energy decreases by 16.087 and 61.456%, respectively, under the same situations. Hence, the load angle has a considerable impact on FPL and SEA.

In terms of FPL, it is observed that for the axial impact case, FPL increases in the order of subgroups I-NMHC, II-NMHC, and III-NMHC, due to the increase in the column's number of cells. However, for oblique impacts, the differences in FPL values among the subgroups are minimal. For example, in the case of axial impact, the values of FPLs for I-NMHC1.4–80-0, II-NMHC1.4–80-0, and III-NMHC1.4–80-0 are, respectively, 27.545 kN, 32,479 kN, and 34.043 kN. In the case of oblique impact at 10°, the values of FPLs for the same columns are 7.577 kN, 8.143 kN, and 8.273 kN, respectively, and they are 3.265 kN, 4,115 kN, and 4,101 kN for oblique impact at 20°. For columns within the same subgroup, FPLs of columns with the same thickness increase as their diameters increase. However, the values of FPLs are nearly the same for columns subjected to oblique impact. For example, the FPLs of I-NMHC1.8–70-0, I-NMHC1.8–80-0, and I-NMHC1.8–90-0 are 29.785 kN, 32,421 kN, and 39.116 kN, respectively. The average FPL value for these columns is about 11.699 kN for a load angle of 10° and 6.24 kN for a load angle of 20°. Additionally, FPLs of columns with the same diameter in the same subgroup

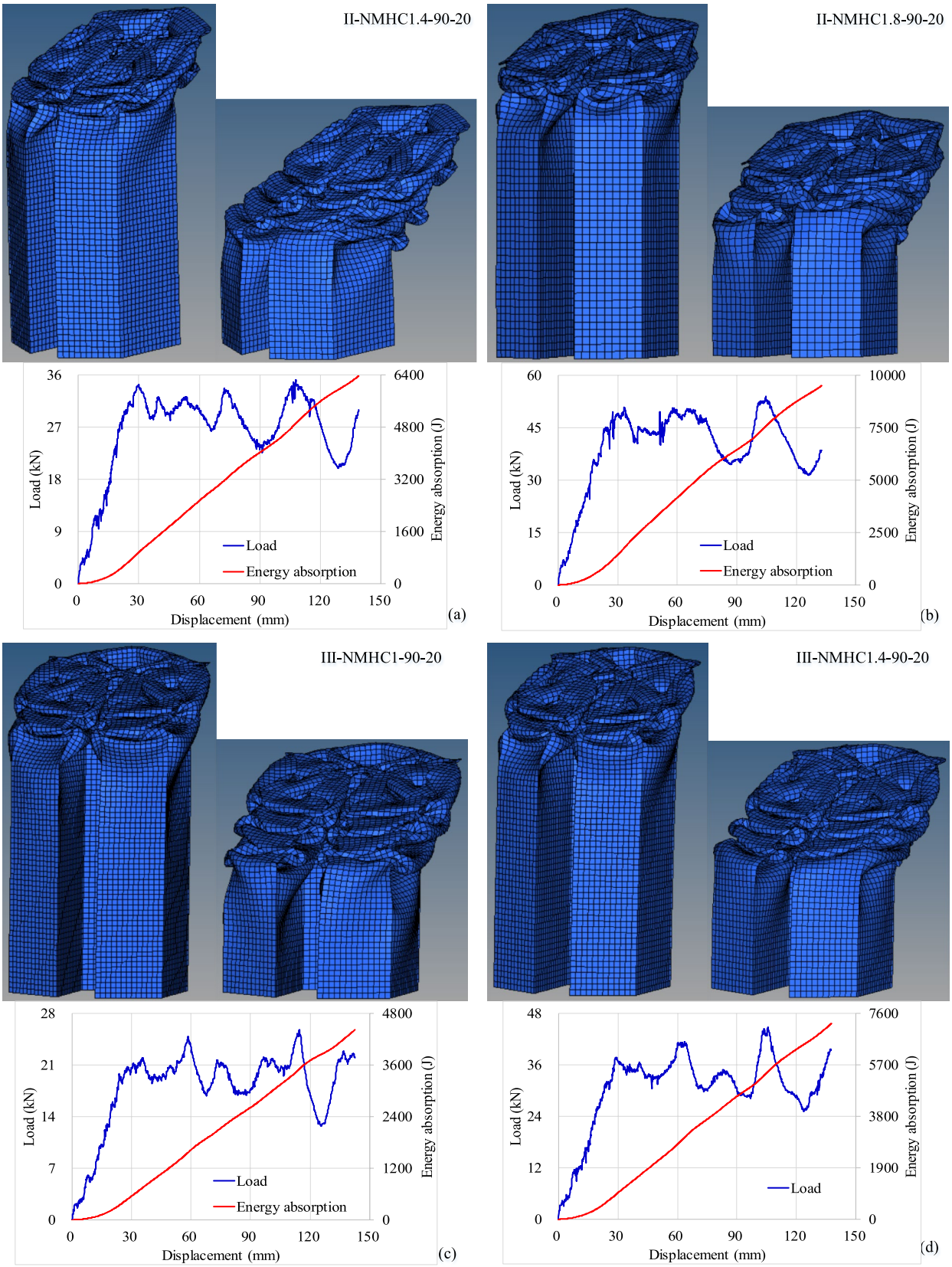

Fig. 9 Behaviors of NMHCs without bending: **a** II-NMHC1.4–90-20, **b** II-NMHC1.8–90-20, **c** III-NMHC1-90–20, and **d** III-NMHC1.4–90-20

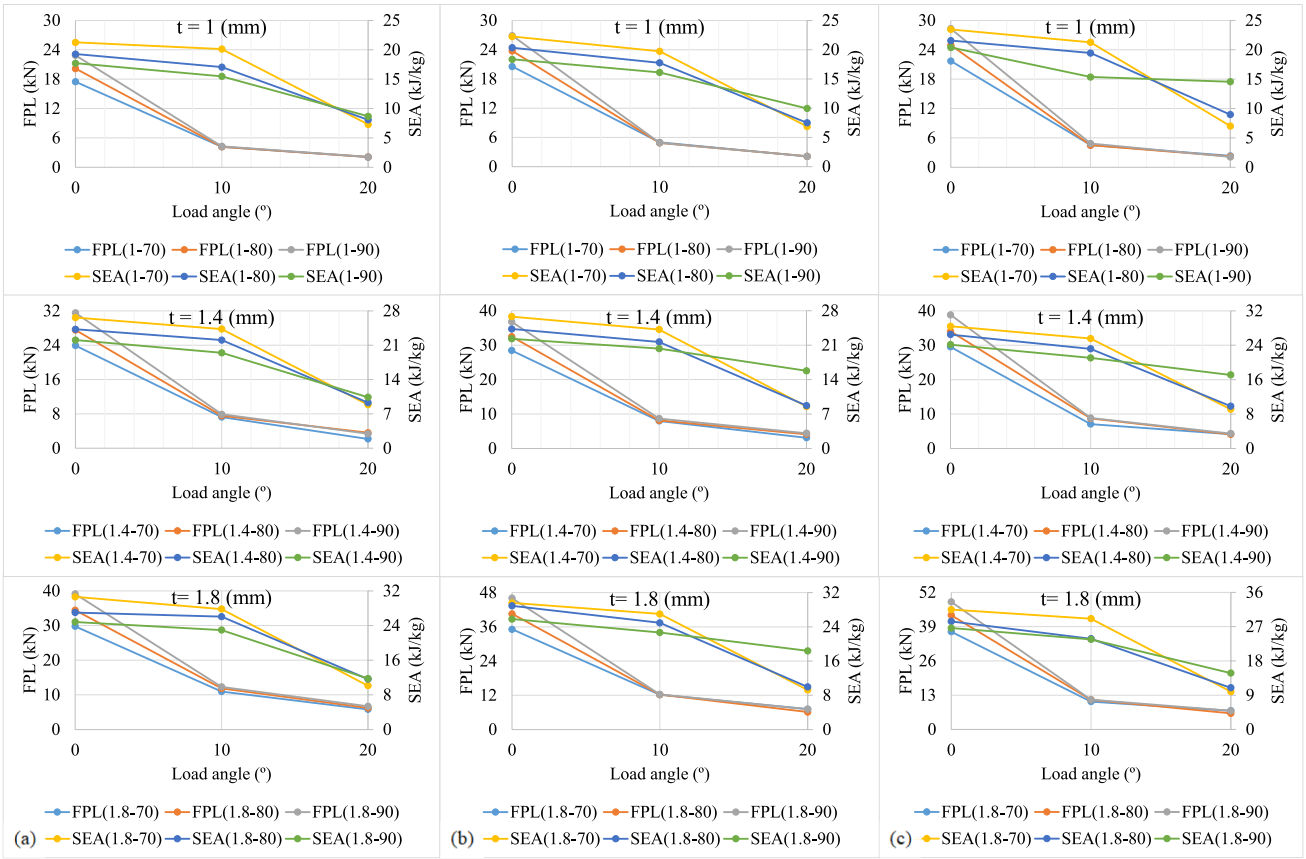

Fig. 10 Variation of crashworthiness indexes: **a** I-NMHC, **b** II-NMHC, and **c** III-NMHC

increase as their wall thicknesses increase, as shown in Fig. 10. For instance, the FPLs of III-NMHC1-70–0, III-NMHC1.4–70, and III-NMHC1.8–70-0 are 22.253 kN, 26.803 kN, and 29.606 kN.

Compared to the variation of FPL, the variation of SEA is relatively small. In all impact cases, SEA increases in order of subgroups I-NMHC, II-NMHC, and III-NMHC due to the mass and section geometry of the columns. However, for specific columns under oblique impacts, SEAs can differ significantly, as shown in Fig. 10. For example, the SEAs of I-NMHC1.4–90-0, II-NMHC1.4–90-0, and III-NMHC1.4–90-0 are 22.055 kJ/kg, 22.288 kJ/kg, and 24.136 kJ/kg, respectively. In the case of oblique impact of 10°, their values are 19.453 kJ/kg, 20.298 kJ/kg, and 21.054 kJ/kg, respectively, and in the case of oblique impact of 20°, they are 10.390 kJ/kg, 15.794 kJ/kg, and 17.100 kJ/kg, respectively. For columns within the same subgroup, the SEAs of those with constant thickness decrease as their diameters increase, whereas those with constant diameter increase as their wall thicknesses increase. For instance, the SEAs of III-NMHC1.4–70-10, III-NMHC1.4–80-10, and III-NMHC1.4–90-10 are 25.558 kJ/kg, 23.169 kJ/kg, and 21.054 kJ/kg, respectively, while those of II-NMHC1-80–10, II-NMHC1.4–80-10, and II-NMHC1.8–80-10 are 17.757 kJ/kg, 21.659 kJ/kg, and 24.944 kJ/kg, respectively.

Furthermore, the results indicate that four columns, namely II-NMHC1.4–90-20, II-NMHC1.8–90-20, III-NMHC1-90–20, and III-NMHC1.4–90-20, exhibited progressive deformation behavior under oblique impact with a large load angle of 20°. In comparison to the case of axial load, their SEAs decreased by an average of 29% in this impact scenario, while the SEAs of other columns decreased by an average of 61.5%, as seen in Figs. 10 and 11, and Tables 1 and 2. This result is consistent with the conclusions of Booth et al. (Booth et al. 2021). Thus, section geometry plays a major role in determining a column's behavior and crashworthiness performance, as does the load angle.

Apart from the load angle and section geometry, tube parameters such as wall thickness and diameter also have a considerable effect on FPL and SEA (Gong et al. 2020). However, tube parameters have a more pronounced impact on FPL than on SEA. An increase in wall thickness and diameter leads to an increase in FPL. For a constant wall thickness, an increase in diameter results in a lower SEA, while for a constant diameter, increasing the wall thickness leads to a larger SEA.

Table 2 Decrease in FPL and SEA

Group				I–NMHC		II–NMHC		III–NMHC	
n	t (mm)	a (mm)	Alpha (°)	FPLE (%)	SEAE (%)	FPLE (%)	SEAE (%)	FPLE (%)	SEAE (%)
1	1.0	70	0	0	0	0	0	0	0
2			10	–76.051	–5.361	–75.753	–11.383	–79.103	–9.345
3			20	–88.000	–65.637	–89.774	–69.169	–89.198	–70.035
4	1.0	80	0	0	0	0	0	0	0
5			10	–79.240	–11.461	–79.522	–12.685	–81.899	–9.820
6			20	–89.526	–58.003	–91.085	–63.169	–91.086	–58.360
7	1.0	90	0	0	0	0	0	0	0
8			10	–81.279	–12.617	–81.879	–12.278	–82.795	–24.657
9			20	–90.693	–50.992	–92.147	–45.756	–92.509	–28.585
10	1.4	70	0	0	0	0	0	0	0
11			10	–69.642	–8.807	–71.899	–9.758	–76.011	–10.072
12			20	–90.913	–66.713	–89.048	–68.127	–85.908	–67.882
13	1.4	80	0	0	0	0	0	0	0
14			10	–72.491	–9.116	–74.929	–10.856	–74.377	–12.520
15			20	–86.841	–61.676	–87.330	–64.129	–87.954	–62.863
16	1.4	90	0	0	0	0	0	0	0
17			10	–74.936	–11.800	–76.382	–8.930	–77.196	–12.768
18			20	–89.302	–52.890	–87.974	–29.137	–88.840	–29.150
19	1.8	70	0	0	0	0	0	0	0
20			10	–63.228	–9.219	–65.246	–8.758	–71.501	–7.604
21			20	–80.501	–66.956	–79.683	–68.721	–80.846	–68.428
22	1.8	80	0	0	0	0	0	0	0
23			10	–65.593	–3.563	–69.858	–13.772	–74.053	–16.087
24			20	–81.931	–56.927	–84.898	–65.549	–85.913	–61.456
25	1.8	90	0	0	0	0	0	0	0
26			10	–68.550	–7.537	–73.284	–12.108	–76.675	–11.177
27			20	–82.889	–52.608	–84.513	–28.735	–85.360	–44.436

4.3 Optimization result

In this study, multi-objective optimization was performed using Isight 2018 Design Gateway (Dassault Systèmes), which integrates response surface methodology (RSM) with the Multi-Objective Particle Swarm Optimization (MOPSO) algorithm. A three-level full factorial design was used to generate 27 sampling points across the design space defined by wall thickness (t), diameter (a), and loading angle (α), as listed in Table 1. The optimization procedure involved three stages: (1) generation of sampling points using the factorial design; (2) construction of RSM models for first peak load (FPL) and specific energy absorption (SEA) based on FEM simulations; and (3) application of MOPSO (Albak et al. 2021) within Isight to identify Pareto-optimal solutions that minimize FPL while maximizing SEA. Model accuracy was assessed using the coefficient of determination (R^2) and adjusted R^2 (R^2adj), with values above 0.9 confirming good predictive reliability (Table 3).

The variations of FPL and SEA with respect to t, a, and α are shown in Fig. 10 for I-, II-, and III-NMHCs. The subgroups exhibit similar behavior within the design domain, with response surfaces showing significant curvature and variation. Based on these surfaces, MOPSO produced Pareto fronts for the three subgroups (Fig. 12), each demonstrating the trade-off between FPL and SEA. The ranges of FPL and SEA were comparable across all subgroups.

Analysis of Figs. 11 and 12 indicates that the optimal load angles fall within 0.15–0.24 rad (~ 8.6–13.8°). The optimal design parameters for the three subgroups are summarized in Table 4, which shows that thickness and diameter values converge due to geometric similarity. Importantly, the preferable load angle that yields low FPL and high SEA is approximately 10°. These findings provide useful guidance for automobile designers in improving crash box performance and enhancing vehicle passive safety.

4.4 Comparison with other multi-cell hexagonal columns

In this section, a comprehensive comparison of III-NMHC with other hexagonal sections, specifically HMHA (Gao

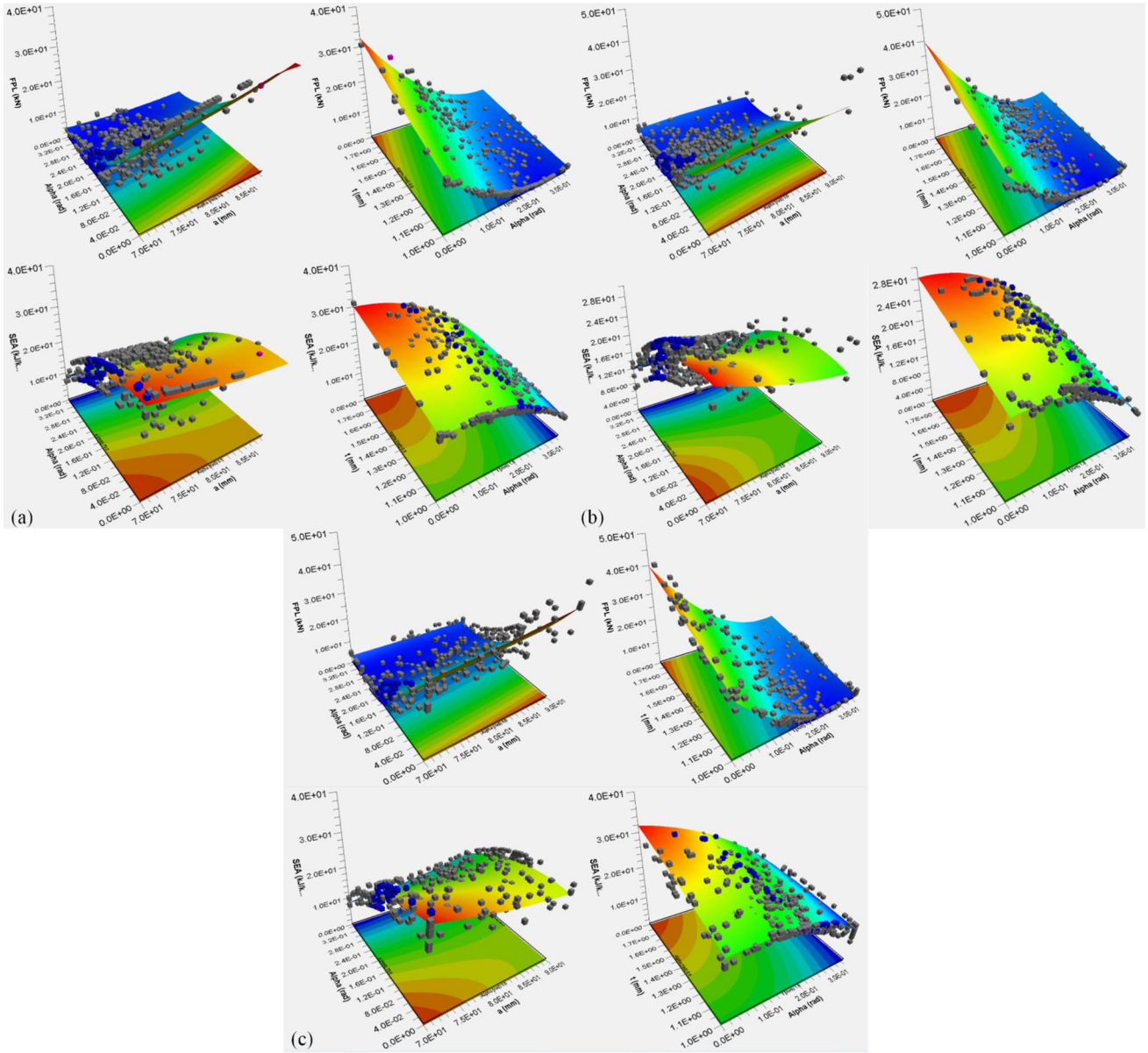

Fig. 11 Response surface: **a** I-NMHC, **b** II-NMHC, and **c** III-NMHC

Table 3 Accuracy evaluation of RS model

Evaluation index	I-NMHC		II-NMHC		III-NMHC	
	FPL	SEA	FPL	SEA	FPL	SEA
R^2	0.9941	0.9854	0.9885	0.9382	0.9929	0.9645
R^2_{adj}	0.9917	0.9776	0.9824	0.9063	0.9885	0.9447
Allowable value	> 0.9					

et al. 2023) and HV1-T1 (Yulong et al. 2022), which share the same features, is performed under loading conditions of axial loading and oblique loadings of 10° and 20°. All these columns, with an outer diameter of 70 mm, have the same mass and wall thickness.

The deformation responses of these columns under various loading conditions, as illustrated in Fig. 13, demonstrated consistent compact-mode deformation patterns characterized by similar folding mechanisms and progressive deformation features. Notably, none of the

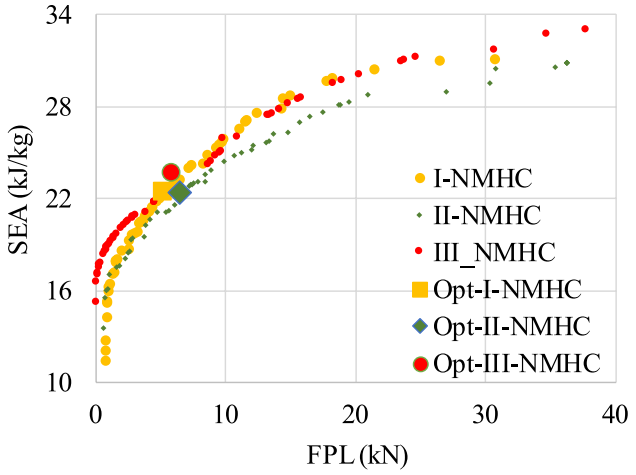

Fig. 12 Pareto fronts for three subgroups

Table 4 Optimum

Column	a (mm)	Alpha (rad or °)	t (mm)	FPL (kN)	SEA (kJ/kg)
I-NMHC	70	0.184 or 10.56	1.353	5.244	22.404
II-NMHC	70	0.1628 or 9.328	1.295	6.558	22.362
III-NMHC	70.292	0.178 or 10.201	1.384	6.016	23.587

three column designs exhibited global bending behavior, even under the most severe oblique loading condition of 20°. Load-response analysis revealed stable characteristics across all specimens, with a distinctive plateau stage manifesting toward the conclusion of the impact process. Among the tested configurations, III-NMHC consistently demonstrated the highest load levels, while HMHA exhibited the lowest across all loading scenarios.

A detailed comparison of crashworthiness characteristics, presented in Fig. 14, established III-NMHC's superior performance, characterized by minimal First Peak Load (FPL) and maximal Energy Absorption (EA), with minor exceptions observed in oblique impact scenarios at 10° and 20°. These exceptions manifested as marginally higher FPLs, though the variations remained relatively modest—ranging from 0.71 kN to 1.68 kN when compared to HMHA, and from 0.02 kN to 1.44 kN relative to HV1-T1. In terms of Energy Absorption capacity, III-NMHC demonstrated remarkable advantages: a 14.14% enhancement under axial impact and approximately 18.5% improvement under oblique impact conditions compared to HMHA, while achieving increases of 13.02% and approximately 19%, respectively, when measured against HV1-T1.

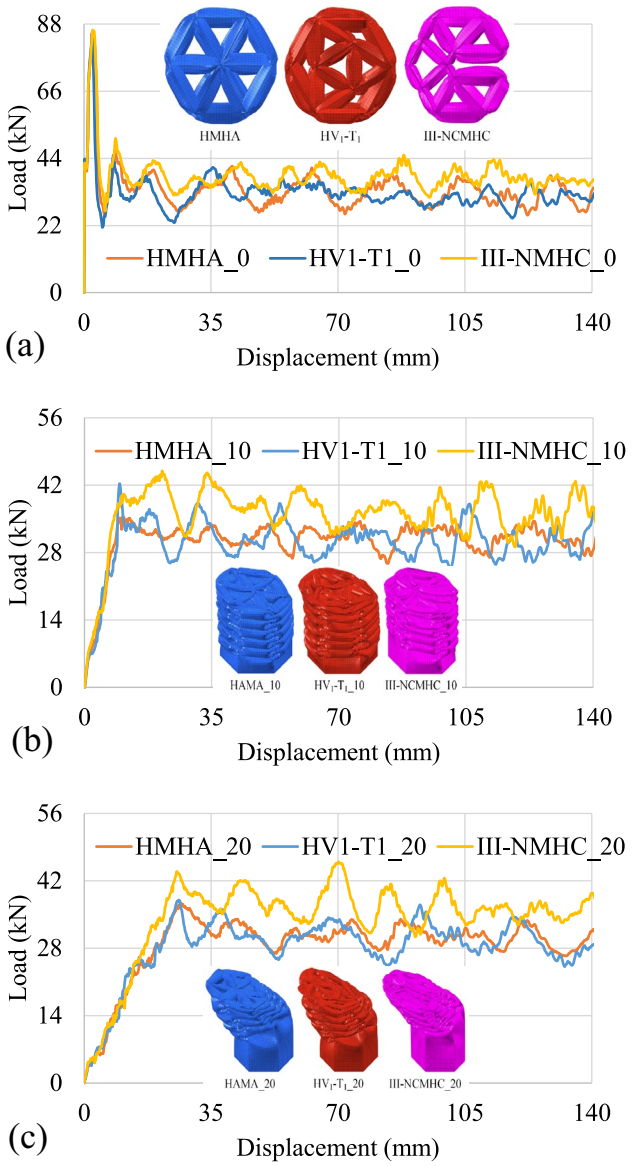

Fig. 13 Behaviors of HMHA (Gao et al. 2023), HV1-T1 (Yulong et al. 2022), and III-NMHC: **a** under axial loading, **b** oblique loading of 10°, and **c** oblique loading of 20°

5 Conclusion

This study evaluated the crashworthiness of non-closed multi-cell hexagonal columns (NMHCs) with novel cross-sections derived from topology optimization. Using FEM and multi-objective optimization, the effects of wall thickness, diameter, and loading angle on peak load and specific energy absorption were systematically examined.

The results show that crashworthiness performance is highly sensitive to loading angle, with an optimum at 10°. Group II NMHCs achieved progressive deformation with thicker walls, while Group III favored thinner walls, demonstrating that both cell number and wall thickness govern

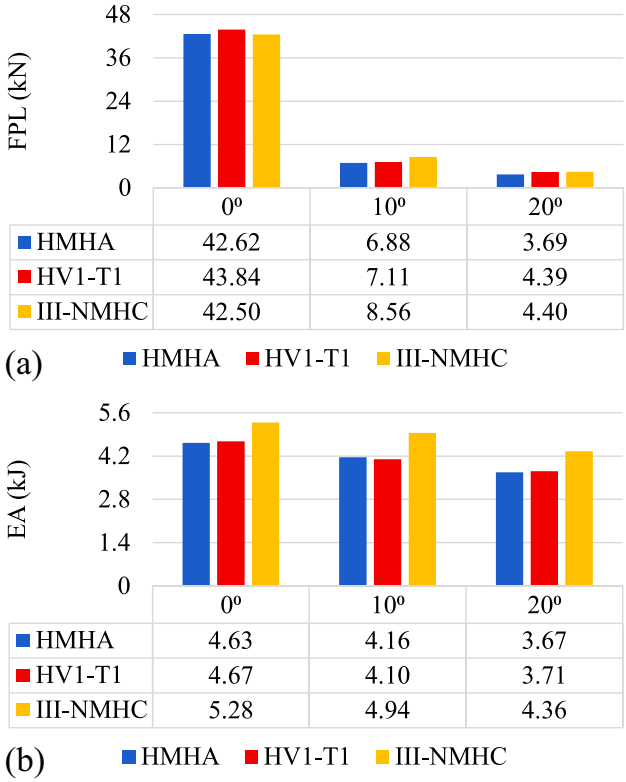

Fig. 14 Crashworthiness indexes of three hexagonal sections

folding stability. Among all variants, III-NMHC specimens exhibited the best balance, with the lowest peak load and highest energy absorption.

These findings highlight load angle, cell number, and section geometry as critical design parameters for improving energy absorption and reducing peak loads in crashworthy structures. The outcomes provide valuable guidelines for the design of lightweight crash boxes to enhance vehicle passive safety.

Author contributions VanThanh Dang: Methodology, Writing – original draft. Michal Rogala: Formal analysis, Review. Ameen Topa: Numerical simulation. PhucThien Nguyen: Analysis of numerical simulation, Data curation. TrongNhan Tran: Conceptualization, Supervision, and Writing-revised draft. All authors read and approved the final manuscript.

Funding The author Michal Rogala acknowledges support of the Scientific Discipline of Mechanical Engineering (Grant no. FD-20/IM-5/091).

Data availability The data supporting the findings of this study are available from the corresponding author upon reasonable request.

Declarations

Conflict of interest The authors declare that there are no conflict of interests regarding the publication of this article.

Replication of Results We can provide the presented results upon reasonable request.

References

Alavi Nia A, Parsapour M (2014) Comparative analysis of energy absorption capacity of simple and multi-cell thin-walled tubes with triangular, square, hexagonal and octagonal sections. Thin-Walled Struct 74:155–165

Albak Eİ (2021) Crashworthiness design for multi-cell circumferentially corrugated thin-walled tubes with sub-sections under multiple loading conditions. Thin Walled Struct 164:107886

Albak Eİ, Solmaz E, Yıldız AR, Öztürk F (2021) Multiobjective crashworthiness optimization of graphene type multi-cell tubes under various loading conditions. J Braz Soc Mech Sci Eng 43(5):266

Ali M, Ohioma E, Kraft F, Alam K (2015) Theoretical, numerical, and experimental study of dynamic axial crushing of thin walled pentagon and cross-shape tubes. Thin-Walled Struct 94:253–272

Arnold B, Altenhof W (2004) Experimental observations on the crush characteristics of AA6061 T4 and T6 structural square tubes with and without circular discontinuities. Int J Crashworthiness 9(1):73–87

Aulig N, Nutwell E, Menzel S, Detwiler D (2018) Preference-based topology optimization for vehicle concept design with concurrent static and crash load cases. Struct Multidisc Optim 57(1):251–266

Bendsøe M, Sigmund O: **Topology optimization. Theory, methods, and applications. 2nd ed., corrected printing**; 2004.

Booth DN, Kohar CP, Inal K (2021) Multi-objective optimization of a multi-cellular aluminum extruded crush rail subjected to dynamic axial and oblique impact loading conditions. Thin-Walled Struct 166:108021

Chen W, Wierzbicki T (2001) Relative merits of single-cell, multi-cell and foam-filled thin-walled structures in energy absorption. Thin-Walled Struct 39(4):287–306

Chen J, Li E, Li Q, Hou S, Han X (2022) Crashworthiness and optimization of novel concave thin-walled tubes. Compos Struct 283:115109. https://doi.org/10.1016/j.compstruct.2021.115109

Chen J, Li E, Liu W, Mao Y, Hou S (2023) Sustainable composites with ultrahigh energy absorption from beverage cans and polyurethane foam. Compos Sci Technol 239:110047

Chen J, Li E, Liu W, Mao Y, Hou S (2024a) Crashworthiness analysis of novel cactus-inspired multi-cell structures under axial crushing. Int J Mech Sci 268:109053

Chen Y, Deng X, Huang H, Ran H, Wang C (2024b) Crashworthiness of bionic tree-shaped hexagonal hierarchical gradient structures under oblique crushing conditions. Mech Adv Mater Struct 31(25):6923–6943

Deng X, Chen Y, Huang J (2024) Crashworthiness analysis of hexagonal hierarchical gradient tubes with axial variable thickness inspired by tree fractal structure. Mech Adv Mater Struct 31(21):5398–5413

Gao Z, Xia F, Li J, Ruan D (2023) Axial compression of multi-cell hexagonal tubes with novel hierarchical architectures: numerical and theoretical analyses. Compos Struct 318:117079

Gong C, Bai Z, Lv J, Zhang L (2020) Crashworthiness analysis of bionic thin-walled tubes inspired by the evolution laws of plant stems. Thin-Walled Struct 157:107081

Gong C, Hu Y, Bai Z (2023) Crashworthiness analysis and optimization of lotus-inspired bionic multi-cell circular tubes. Mech Adv Mater Struct 30(24):4996–5014

Hou S, Li Q, Long S, Yang X, Li W (2008) Multiobjective optimization of multi-cell sections for the crashworthiness design. Int J Impact Eng 35(11):1355–1367

Hou S, Han X, Sun G, Long S, Li W, Yang X, Li Q (2011) Multiobjective optimization for tapered circular tubes. Thin Walled Struct 49(7):855–863

Hou S, Zhang Z, Yang X, Yin H, Li Q (2014) Crashworthiness optimization of new thin-walled cellular configurations. Eng Comput 31(5):879–897

Huang H, Xu S (2019) Crashworthiness analysis and bionic design of multi-cell tubes under axial and oblique impact loads. Thin-Walled Struct 144:106333. https://doi.org/10.1016/j.tws.2019.106333

Isaac CW, Oluwole O (2018) Structural response and performance of hexagonal thin-walled grooved tubes under dynamic impact loading conditions. Eng Struct 167:459–470

Jiang Z, Zhao J, Xing S, Sun X, Qu M, Lv H (2024) Crashworthiness design and multi-objective optimization of 3D-printed carbon fiber-reinforced nylon nested tubes. Polym Compos 45(12):11289–11311

Lam L, Chen W, Hao H, Li Z, Ha NS (2023) Dynamic crushing performance of bio-inspired sandwich structures with beetle forewing cores. Int J Impact Eng 173:104456

Latifi Rostami SA, Ghoddosian A (2019) Topology optimization under uncertainty by using the new collocation method. Period Polytech Civ Eng 63(1):278–287

Li Z, Duan L, Chen T, Hu Z (2018) Crashworthiness analysis and multi-objective design optimization of a novel lotus root filled tube (LFT). Struct Multidiscip Optim 57(2):865–875

Li Z, Rakheja S, Shangguan W-B (2019) Crushing behavior and crashworthiness optimization of multi-cell square tubes under multiple loading angles. Proc Inst Mech Eng Pt D J Automob Eng 234(5):095440701986912. https://doi.org/10.1177/0954407019869127

Liu J, Wen G, Huang X (2017) To avoid unpractical optimal design without support. Struct Multidisc Optim 56(6):1589–1595

Liu W, Jin L, Luo Y, Deng X (2021) Multi-objective crashworthiness optimisation of tapered star-shaped tubes under oblique impact. Int J Crashworthiness 26(3):328–342

McGregor LJ, Meadows DJ, Scott CE, Seeds AD: **Impact performance of aluminium structures in Structural Crashworthiness and Failure (Jones N and Wierzbicki T)**. *Elsevier Science Publisher* 1993.

Nikkhah H, Guo F, Chew Y, Bai J, Song J, Wang P (2017) The effect of different shapes of holes on the crushing characteristics of aluminum square windowed tubes under dynamic axial loading. Thin-Walled Struct 119:412–420

Nikkhah H, Crupi V, Baroutaji A (2020) Crashworthiness analysis of bio-inspired thin-walled tubes based on Morpho wings microstructures. Mech Based des Struct Mach. https://doi.org/10.1080/15397734.2020.1822184

Olabi AG, Morris E, Hashmi MSJ (2007) Metallic tube type energy absorbers: a synopsis. Thin-Walled Struct 45(7–8):706–726

Peng Y, Li T, Hou L, Wang K, Xie G, Zhang H (2024) Bio-inspired cellular thin-walled structures under impact loading: modeling and multi-stage cooperative optimization algorithm. Mech Adv Mater Struct 31(19):4737–4754

Pirmohammad S, Esmaeili-Marzdashti S (2019) Multi-objective crashworthiness optimization of square and octagonal bitubal structures including different hole shapes. Thin-Walled Struct 139:126–138

Pirmohammad S, Vosoughifard E (2024) Crashworthiness behavior of multi-cell structures reinforced with small tubes under axial and inclined loading. Mech Based Design Struct Mach 52(12):10783–808

Qi C, Yang S, Dong F (2012) Crushing analysis and multiobjective crashworthiness optimization of tapered square tubes under oblique impact loading. Thin-Walled Struct 59:103–119

Qin S, Deng X, Liu F (2024) Crashworthiness of double-gradient hierarchical hexagonal tubes under multiple loads. Mech Adv Mater Struct 31(18):4325–4342

Reid SR (1993) Plastic deformation mechanisms in axially compressed metal tubes used as impact energy absorbers. Int J Mech Sci 35(12):1035–1052

Song J, Xu S, Liu S, Zou M (2020) Study on the crashworthiness of bio-inspired multi-cell tube under axial impact. Int J Crashworthiness. https://doi.org/10.1080/13588265.2020.1807686

Tarlochan F, Samer F, Hamouda AMS, Ramesh S, Khalid K (2013) Design of thin wall structures for energy absorption applications: enhancement of crashworthiness due to axial and oblique impact forces. Thin-Walled Struct 71:7–17

Tran T, Baroutaji A (2018) Crashworthiness optimal design of multicell triangular tubes under axial and oblique impact loading. Eng Fail Anal 93:241–256

Tran T, Hou S, Han X, Nguyen N, Chau M (2014) Theoretical prediction and crashworthiness optimization of multi-cell square tubes under oblique impact loading. Int J Mech Sci 89:177–193

Tran T, Eyvazian A, Estrada Q, Le D, Nguyen N, Le H (2020) Lateral behaviors of nested tube systems under quasi-static condition. Int J Appl Mech 12(04):2050046

Waleed I, Ruhaima AAK, Farhan ZA, Ismael NS, Alhassan MS, Skikara M, Albahash ZF, Ahmed AN (2023) Investigating energy absorption of thin-walled steel structures with combined mechanisms including inversion, folding and expansion. Proc Instit Mech Eng, Part l: J Mater: Design Appl. https://doi.org/10.1177/14644207231173053

Xiang J, Du J (2017) Energy absorption characteristics of bio-inspired honeycomb structure under axial impact loading. Mater Sci Eng A Mater Struct Prop Microstruct Process 696:283–289

Xiong J, Zhang Y, Su L, Zhang F, Wu C (2022) Experimental and numerical study on mechanical behavior of hybrid multi-cell structures under multi-crushing loads. Thin-Walled Struct 170:108588. https://doi.org/10.1016/j.tws.2021.108588

Xu X, Zhang Y, Wang J, Jiang F, Wang CH (2018) Crashworthiness design of novel hierarchical hexagonal columns. Compos Struct 194:36–48

Yang M, Han B, Su P-B, Wei Z-H, Zhang Q, Zhang Q-C, Lu TJ (2019) Axial crushing of ultralight all-metallic truncated conical sandwich shells with corrugated cores. Thin-Walled Struct 140:318–330

Yu X, Pan L, Chen J, Zhang X, Wei P (2019) Experimental and numerical study on the energy absorption abilities of trabecular–honeycomb biomimetic structures inspired by beetle elytra. J Mater Sci 54(3):2193–2204

Yulong H, Tao J, Xin L, Ji Q, Xuefeng S (2022) Crashworthiness design of hexagonal tubes using self-similar inspired structures. Mater Today Commun 33:104934

Zhang L, Bai Z, Bai F (2018) Crashworthiness design for bio-inspired multi-cell tubes with quadrilateral, hexagonal and octagonal sections. Thin-Walled Struct 122:42–51